An Effective Neural Network-Boundary Integral Approach for the Analysis of Natural Convection Flow

Nam Mai-Duy and Thanh Tran-Cong*

Faculty of Engineering and Surveying,

University of Southern Queensland, Toowoomba, QLD 4350, Australia

Submitted to Intl. J. Numer. Meth. Fluids, 16 April 2003

*Corresponding author: Telephone +61 7 46312539, Fax +61 7 46 312526, E-mail trancong@usq.edu.au

SUMMARY

This paper presents a new neural network-boundary integral approach for the analysis of natural convection flow. The use of integral equations (IEs) allows the set of simultaneous unknowns to be confined to the boundary only. In this study, all boundary values including geometries are represented by indirect radial basis function networks (IRBFNs), resulting in an effective boundary element method (BEM) especially for the achievement of high Rayleigh numbers with relatively coarse and uniform meshes. Convergence is obtained up to a Rayleigh number of $1.0e7$ in the case of a square cavity using a uniform mesh of 31×31 and a Rayleigh number of $5.0e4$ in the case of a horizontal concentric annulus using a uniform mesh of 11×21.

KEY WORDS: boundary element method, natural convection flow, indirect radial basis function network.

1 Introduction

Heat transfer by natural convection in enclosed spaces has found many applications in engineering, such as nuclear reactor design, double glazing, cooling of electronic equipment, aircraft cabin insulation, solar energy collection and thermal storage systems. As a result, much experimental and theoretical work has been devoted to this topic in recent decades. In the context of numerical simulation, natural convective heat transfer problems have been simulated by a wide range of numerical methods, e.g. the indirect RBFN based method (Mai-Duy and Tran-Cong [1]), the differential quadrature method (Shu [2]; Shu and Zhu [3]), FDM (Kuehn and Goldstein [4]; Projahn et al [5]; De Vahl Davis [6]), FEM (Sammouda et al [7]; Manzari [8]), FVM (Glakpe et al [9]; Kaminski and Prakash [10]) and BEM (Kitagawa et al [11]; Hribersek and Skerget [12]; Power and Mingo [13]).

The boundary element method (BEM) has become a powerful technique for solving partial differential equations (PDEs) in science and engineering (Banerjee and Butterfield [14]; Brebbia et al [15]). An advantage of the method is the reduction of the dimension of the solution space by one unit. For linear problems, e.g. potential problems governed by the Laplace equation or creeping viscous flows governed by the Stokes equation, it is not necessary to compute the requisite function throughout the domain of solution. In addition the internal values here are represented in an exact form, making the BEM vastly superior in terms of efficiency and accuracy in comparison with the FDM and the FEM (Pozrikidis [16]). However, for nonlinear problems such as non-zero Reynolds number viscous flows governed by the Navier-Stokes equation or heat transfer problems governed by the Poisson equation, the above powers of the BEM weaken due to the lack of the corresponding fundamental solutions. Consequently, some adjustments are necessary. Nonlinear terms now need be lumped together to form a "known" forcing function (pseudo body force) so that the well-known BEM with the fundamental point force solution for linear problems can be extended to solve nonlinear ones (Bush and Tanner [17]). As a result, an iterative

process needs be employed to render nonlinear terms linear. Furthermore, the pseudo body forces are accounted for in the boundary element formulations as volume integrals, which normally require a discretisation of the full domain for computation. However, for the latter, with the introduction of reference velocities and temperatures together with the application of the divergence theorem, volume modelling can often be confined to only a small portion of the problem domain, typically near obstacles or walls (Dargush and Banerjee [18]). An alternative is to use meshless techniques such as the DRM (Partridge et al [19]) and the particular solutions (Zheng et al [20]) to transform volume integrals into surface integrals, resulting in a true BIE formulation. Nevertheless, the BEM is still attractive for solving certain classes of problems without large storage requirements.

The governing equations of natural convection represent coupling between the temperature and velocity fields and involve strong nonlinearities. The momentum equation and the energy equation here must be solved simultaneously. Onishi et al [21] proposed a boundary element formulation in terms of stream-function, vorticity and temperature as variables for the natural convection problem. Accurate solutions of a square cavity problem were obtained only at low Rayleigh numbers ($Ra \leq 1.0e4$) (Kitagawa et al [11]). Skerget et al [22] employed the velocity-vorticity-temperature and velocity-vorticity-pressure-temperature IE formulations for the simulation of thermally driven cavity flow and found that the latter produced more stable results. Two uniform meshes of 11×11 and 21×21 with linear boundary elements and linear triangular cells were employed and the results were reported for a Rayleigh number up to $1.0e5$. In Kitagawa et al's work [11], a boundary element formulation in terms of the primitive variables, i.e. velocity and pressure, in conjunction with the use of a penalty function technique was developed. In that work, the gradients of velocity and temperature were calculated directly by differentiating the corresponding integral equations. With non-uniform discretisation using 132 boundary nodes and 169 internal nodes for linear boundary elements and linear triangular cells, the converged solutions were obtained up to $Ra = 1.e4$ (an attempt at higher

Rayleigh number of $1.0e5$ failed to converge). Later on, Kitagawa [23] pointed out the necessity of using higher order cells to improve the solution accuracy and also to achieve convergence. Non-uniform discretisation, with quadratic quadrilateral cells and linear boundary elements using 164 boundary nodes and 315 internal points, was employed and convergence was achieved up to $Ra = 1.0e6$. Note that the value of a penalty parameter was recommended to be of the order of $1.0e4$ to $1.0e5$ in practice. Lower or higher values can make the results less accurate or the iteration cycle unstable respectively. From another point of view, the BEM has also been incorporated with domain decomposition techniques, where the integral representation formulae are applied to subdomains and a system of equations is then formed from the assembly of subdomain matrices using the continuity conditions across common interfaces. The advantages of this approach are that the resultant coefficient matrix is sparse/block-banded and its solution is more efficient. However, such an approach with a relatively large number of subdomains is somewhat akin to the finite element method. Power and Mingo [13] have applied the dual reciprocity sub-domain decomposition approach for the analysis of natural convection flow in a square cavity. The domain integrals in each subdomain are transformed into surface integrals via the DRM. This approach achieved convergence up to a Rayleigh number of $2.0e4$ using 16 uniform sub-regions with 48 surface quadratic elements and 100 internal points uniformly distributed in each sub-region. The authors reported that beyond this value of Rayleigh number, problems associated with convergence appeared.

Recently, Mai-Duy and Tran-Cong [24,25] have shown that the indirect radial basis function networks (IRBFNs) perform better than element-based methods for function interpolation. The IRBFNs were then successfully introduced into the BEM scheme to represent boundary values for the analysis of viscous flow in a lid-driven cavity (Mai-Duy and Tran-Cong [26]). In this paper, the IRBFN-BEM approach is extended to analyse natural convection flows. It is shown that the approximation of the boundary values by IRBFNs significantly improves the performance of the BEM in terms of higher Rayleigh number

attainment and accuracy of the solution. To demonstrate that the improved performance of the BEM is owing to the use of the IRBFN interpolations to represent the variations of functions (velocity, traction, temperature, heat flux and geometry) along the boundary, all other aspects of the analysis are kept the same, i.e. a single domain, the use of the Stokeslet fundamental solution (the primitive variables) and the standard treatments for the convective terms by a successive substitution scheme and linear triangular cell approximations. The present IRBFN-BEM can achieve a high Rayleigh number value of $1.0e7$ using a relatively coarse and uniform mesh of 31×31 in the case of a square cavity, and $5.0e4$ using a uniform mesh of 11×21 in the case of a horizontal concentric annulus. For the former problem, convergence was observed to be very slow for Rayleigh number above $1.0e7$ which is here considered as a limit of the present approach. The remainder of the paper is organised as follows. In section 2, the governing differential equations of natural convection problem and the corresponding boundary integral formulations are summarised. A brief review of the indirect RBF networks is given in section 3. The proposed IRBFN-BEM scheme for the analysis of natural convection is presented in section 4. Sections 5 and 6 are to verify the validity of the present method through the simulation of natural convection flow for a wide range of Rayleigh numbers in a square cavity and in a horizontal concentric annulus respectively. Section 7 gives some concluding remarks.

2 Governing equations

Consider the two dimensional, steady-state, laminar, buoyancy-induced flow of an incompressible fluid of density ρ and viscosity μ. With the employment of Boussinesq approximation, i.e. the fluid is assumed to have constant properties except for the generation of buoyant force, the equations for the conservation of mass, momentum and energy

take the forms

$$u_{i,i} = 0, \tag{1}$$

$$\mu u_{i,jj} - p_{,i} = \rho u_j u_{i,j} - \rho g_i \eta(\theta - \theta_0), \tag{2}$$

$$k\theta_{,jj} = \rho c_p u_j \theta_{,j}, \tag{3}$$

where tensor notation is used, the indices following a comma denote partial derivatives in space, u_i the velocity vector, p the pressure, θ the temperature, θ_0 the reference temperature, g_i the gravitational acceleration vector, η the coefficient of volumetric expansion, k the thermal conductivity, c_p the specific heat and $\rho g_i \eta(\theta - \theta_0)$ the buoyant force vector. The problem is non-dimensionalised with reference quantities for length, velocity and temperature being the enclosure width L, the thermal diffusion speed α/L, where $\alpha = k/\rho c_p$ is the thermal diffusivity, and the temperature of a cold wall θ_c ($\theta_0 = \theta_c$), respectively, as follows

$$x_i' = \frac{x_i}{L}, \quad u_i' = \frac{u_i}{\alpha/L}, \quad \theta' = \frac{\theta - \theta_c}{\theta_h - \theta_c} \quad \text{and} \quad p' = \frac{pL^2}{\mu\alpha},$$

in which θ_h is the temperature of a hot wall. The resulting dimensionless governing equations, valid under Boussinesq conditions, are given as follows

$$u_{i,i}' = 0, \tag{4}$$

$$u_{i,jj}' - p_{,i}' = \frac{1}{Pr} u_j' u_{i,j}' + Ra\theta' m_i, \tag{5}$$

$$\theta_{,jj}' = u_j' \theta_{,j}', \tag{6}$$

where $m_i = [0, -1]^T$ is the unit vector in the direction of gravity. The independent dimensionless parameters appearing in the equations are respectively the Rayleigh number,

the Prandtl number and the Grashop number

$$Ra = \frac{\eta g(\theta_h - \theta_c)L^3}{\nu\alpha}, \qquad Pr = \frac{\nu}{\alpha}, \qquad Gr = Ra/Pr,$$

where $\nu = \mu/\rho$ is the kinematic viscosity.

Equations (1)-(2) can be reformulated in terms of integral equations for a given spatial point $\mathbf{y} \in \Gamma$ as follows

$$\begin{aligned} c_{ij}(\mathbf{y})u_j(\mathbf{y}) &= \int_\Gamma U_{ij}(\mathbf{y},\mathbf{x})t_j(\mathbf{x})d\Gamma(\mathbf{x}) - \\ &\quad \text{CPV}\int_\Gamma T_{ij}(\mathbf{y},\mathbf{x})u_j(\mathbf{x})d\Gamma(\mathbf{x}) - \rho\int_\Omega U_{ij}(\mathbf{y},\mathbf{x})b_j(\mathbf{x})d\Omega(\mathbf{x}), \qquad (7) \\ U_{ij}(\mathbf{y},\mathbf{x}) &= \frac{1}{4\pi\mu}\left[\frac{r_i}{r}\frac{r_j}{r} - \delta_{ij}\ln(r)\right], \qquad (8) \\ T_{ij}(\mathbf{y},\mathbf{x}) &= -\frac{1}{\pi r}\left[\frac{r_i}{r}\frac{r_j}{r}\frac{\partial r}{\partial n}\right], \qquad (9) \end{aligned}$$

where CPV is Cauchy Principal Value, $\mathbf{x}$ the field point, U_{ij} and T_{ij} the Stokeslet fundamental solutions, u_j and t_j the velocity and the traction vectors respectively, $b_i = u_j u_{i,j} - g_i\eta(\theta - \theta_0)$ the pseudo-body force vector containing the nonlinear acceleration term and the buoyant force, c_{ij} the free term which is $0.5\delta_{ij}$ if the boundary is smooth, $r_i = x_i - y_i$, $r = \|\mathbf{x} - \mathbf{y}\|$ and n is the direction of the outwardly unit vector normal to the boundary. If $\mathbf{y}$ is an interior point then $c_{ij} = \delta_{ij}$ and the second integral on the RHS of (7) is a normal integral (i.e. not a CPV one).

Equation (3) can be regarded as a Poisson's equation here and hence it can also be transformed into an integral formulation as follows. For $\mathbf{y} \in \Gamma$,

$$c(\mathbf{y})\theta(\mathbf{y}) + \text{CPV}\int_\Gamma q^*(\mathbf{y},\mathbf{x})\theta(\mathbf{x})d\Gamma(\mathbf{x}) + \int_\Omega b(\mathbf{x})u^*(\mathbf{y},\mathbf{x})d\Omega(\mathbf{x}) = \int_\Gamma u^*(\mathbf{y},\mathbf{x})q(\mathbf{x})d\Gamma(\mathbf{x}), \qquad (10)$$

where θ and $q = \partial\theta/\partial n$ are the temperature and its gradient respectively, n the direction of the outwardly unit vector normal to the boundary, $b = u_j\theta_{,j}/\alpha$ the source function of

a Poisson's equation, u^* is the fundamental solution to the Laplace equation, e.g. for a two dimensional isotropic domain $u^* = (1/2\pi)\ln(1/r)$ in which r is the distance from the point $\mathbf{y}$ to the current point of integration $\mathbf{x}$, $q^* = \partial u^*/\partial n$, $c(\mathbf{y}) = 1/2$ if the boundary is smooth. If $\mathbf{y}$ is an interior point then $c(\mathbf{y}) = 1$ and the first integral on the LHS of (10) is a normal integral (i.e. not a CPV one).

3 IRBFN interpolation

Radial basis function networks (RBFNs) for approximation and interpolation of function have received a great deal of attention over the last few decades (e.g. Haykin [27]). The RBF network allows a conversion of a function to be approximated from a low dimension space (e.g. 1D-3D) to a high dimension space in which the function can now be expressed as a linear combination of radial basis functions

$$y(\boldsymbol{x}) \approx f(\boldsymbol{x}) = \sum_{i=1}^{m} w^{(i)} g^{(i)}(\boldsymbol{x}), \tag{11}$$

where m is the number of radial basis functions, $\{g^{(i)}\}_{i=1}^{m}$ is the set of chosen radial basis functions and $\{w^{(i)}\}_{i=1}^{m}$ is the set of weights to be found. It has been proved that RBFNs with one hidden layer are capable of universal approximation (Girosi and Poggio [28] and Park and Sandberg [29]) and as a result, RBFNs found application in many disciplines. In the field of numerical solution of PDEs, some RBFNs were successfully used in the boundary element method to transform the volume integrals into equivalent boundary integrals (Zheng et al [20]; Power and Partridge [30]). Furthermore, the networks were also developed successfully to solve PDEs in procedures which are regarded as truly mesh-free methods (e.g. Kansa [31]; Zerroukat et al [32]; Mai-Duy and Tran-Cong [33,1,24]). However, it should be noted that it is still very hard to achieve such an universal approximation RBFN in practice due to the difficulties associated with choosing

the network parameters such as the number of radial basis functions, their positions and widths. In previous works, Mai-Duy and Tran-Cong [24,25] proposed indirect RBFNs (IRBFNs) which are based on the integration process, and their results showed that the IRBFNs perform better than the usual direct RBFNs (DRBFNs) in terms of accuracy and convergence rate for both function and its derivatives. In this paper, the IRBFN is introduced into the BEM scheme to approximate the boundary solution for the analysis of 2D steady natural convection flow problems. In contrast to previous works (Mai-Duy and Tran-Cong [33,1,24]) where the neural networks were used to approximate globally (meshless) the strong form of the governing equations (PDE's), the present work deals with the use of neural networks in the boundary element part of the mesh which discretises the inverse statement of the governing equations. In view of the fact that the BEM allows the reduction of the problem dimensionality by one, only the IRBFN for function and its derivatives (e.g. up to the second order) in 1D needs to be employed here and its formulation with multiquadrics (MQ) is briefly recaptured as follows

$$y''(s) \approx f''(s) = \sum_{i=1}^{m} w^{(i)} g^{(i)}(s), \tag{12}$$

$$y'(s) \approx f'(s) = \sum_{i=1}^{m} w^{(i)} H^{(i)}(s) + C_1, \tag{13}$$

$$y(s) \approx f(s) = \sum_{i=1}^{m} w^{(i)} \bar{H}^{(i)}(s) + C_1 s + C_2, \tag{14}$$

where s is the curvilinear coordinate (arclength), C_1 and C_2 are constants of integration and

$$g^{(i)}(s) = \left((s - c^{(i)})^2 + a^{(i)2}\right)^{1/2}, \tag{15}$$

$$H^{(i)}(s) = \int g^{(i)}(s) ds = \frac{(s - c^{(i)}) \left((s - c^{(i)})^2 + a^{(i)2}\right)^{1/2}}{2} + \frac{a^{(i)2}}{2} \ln \left((s - c^{(i)}) + \left((s - c^{(i)})^2 + a^{(i)2}\right)^{1/2}\right), \tag{16}$$

$$\bar{H}^{(i)}(s) = \int H^{(i)}(s)ds = \frac{((s-c^{(i)})^2 + a^{(i)2})^{3/2}}{6} + \frac{a^{(i)2}}{2}(s-c^{(i)}) \ln\left((s-c^{(i)}) + \left((s-c^{(i)})^2 + a^{(i)2}\right)^{1/2}\right) - \frac{a^{(i)2}}{2}\left((s-c^{(i)})^2 + a^{(i)2}\right)^{1/2}, \tag{17}$$

in which $\{c^{(i)}\}_{i=1}^{m}$ is the set of centres and $\{a^{(i)}\}_{i=1}^{m}$ is the set of RBF widths. The RBF width is chosen based on the following simple relation

$$a^{(i)} = \beta d^{(i)},$$

where β is a factor and $d^{(i)}$ is the minimum arclength between the ith centre and its neighbouring centres. The factor β is simply chosen to be unity in all numerical examples in the present study. Since C_1 and C_2 are to be found, it is convenient to let $w^{(m+1)} = C_1$, $w^{(m+2)} = C_2$, $\bar{H}^{(m+1)} = s$ and $\bar{H}^{(m+2)} = 1$ in (14) which becomes

$$y(s) \approx f(s) = \sum_{i=1}^{m+2} w^{(i)} \bar{H}^{(i)}(s), \tag{18}$$

$$\bar{H}^{(i)} = \text{RHS of (17)}, \quad i = 1, \ldots, m, \tag{19}$$

$$\bar{H}^{(m+1)} = s, \tag{20}$$

$$\bar{H}^{(m+2)} = 1. \tag{21}$$

The detailed implementation and accuracy of the IRBFN method were reported previously (Mai-Duy and Tran-Cong [24,25]). In the following section, the IRBFN is coupled with boundary integral equations for analysis of natural convection flows.

4 IRBFN-BI approach for natural convection

4.1 Introduction of IRBFNs into the BEM scheme

Integral equations allow the solving process to be largely confined to the boundary. After the process is done, the boundary solution obtained provides sources to compute the interior solution. It can be seen that the accuracy of the boundary solution greatly affects the accuracy of the overall solution. As mentioned earlier, neural networks are able to approximate continuous functions arbitrarily well. In this section, the IRBFNs are employed to represent the boundary solution. For simplicity of notation, the volume integrals in (7) and (10) are denoted by VIm and VIe, respectively, in the following discussion.

In the standard BEM, local interpolations are used to approximate the boundary solution via a subdivision of the boundary Γ into a number of small elements. On each element, the geometry and the variations of the functions are assumed to have a certain shape such as linear and quadratic ones. The CPV integrals can be indirectly computed by applying equation (7) to represent rigid body displacements and equation (10) with the hypothesis of a constant potential over the whole domain, while the weakly singular ones can be evaluated using well-known techniques such as the logarithmic Gaussian quadrature and Telles' transformation technique (Telles [34]).

In the present method, global approximations using IRBFNs are employed. The boundary is also divided into a (smaller) number of segments of much larger size, provided that the associated boundaries are smooth and the prescribed boundary conditions are of the same type. On each segment, the variations of the functions (u_j, t_j, θ and q) and the curved geometry (if it exists) are approximated by neural networks. Due to the fact that none of the basis functions employed in the network are null at the singular point (the point

where the field point $\mathbf{x}$ and the source point $\mathbf{y}$ coincide), the method for evaluating the CPV integrals in the standard BEM cannot be applied directly here. To overcome this difficulty, the BIE formulations (7) and (10) need to be rewritten in the form without CPV singularity as follows

$$\int_\Gamma T_{ij}(\mathbf{y},\mathbf{x})\left(u_j(\mathbf{x})-u_j(\mathbf{y})\right)d\Gamma(\mathbf{x}) - \int_\Gamma U_{ij}(\mathbf{y},\mathbf{x})t_j(\mathbf{x})d\Gamma(\mathbf{x}) + VIm = 0, \quad (22)$$

$$\int_\Gamma q^*(\mathbf{y},\mathbf{x})(\theta(\mathbf{x})-\theta(\mathbf{y}))d\Gamma(\mathbf{x}) - \int_\Gamma u^*(\mathbf{y},\mathbf{x})q(\mathbf{x})d\Gamma(\mathbf{x}) + VIe = 0. \quad (23)$$

In the discretised form, equations (22) and (23) become

$$\sum_{k=1}^{N_s}\int_{\Gamma_{(k)}} T_{ij}(\mathbf{y},\mathbf{x})\left(u_{j(k)}(\mathbf{x})-u_{j(l)}(\mathbf{y})\right)d\Gamma_{(k)} - \sum_{k=1}^{N_s}\int_{\Gamma_{(k)}} U_{ij}(\mathbf{y},\mathbf{x})t_{j(k)}(\mathbf{x})d\Gamma_{(k)} + VIm = 0, \quad (24)$$

$$\sum_{k=1}^{N_s}\int_{\Gamma_{(k)}} q^*(\mathbf{y},\mathbf{x})(\theta_{(k)}(\mathbf{x})-\theta_{(l)}(\mathbf{y}))d\Gamma_{(k)}(\mathbf{x}) - \sum_{k=1}^{N_s}\int_{\Gamma_{(k)}} u^*(\mathbf{y},\mathbf{x})q_{(k)}(\mathbf{x})d\Gamma_{(k)}(\mathbf{x}) + VIe = 0, \quad (25)$$

where N_s is the number of segments, subscript (k) denotes general segments and the subscript (l) indicates the segment containing the source point $\mathbf{y}$. The variations of velocity $u_{j(k)}$, traction $t_{j(k)}$, temperature $\theta_{(k)}$ and heat flux $q_{(k)}$ on segment $\Gamma_{(k)}$ are now

represented by IRBFNs in terms of the curvilinear coordinate s as (Equation (18))

$$u_{j(k)} = \sum_{i=1}^{mk+2} w_{u_{j(k)}}^{(i)} \bar{H}_{(k)}^{(i)}(s), \tag{26}$$

$$t_{j(k)} = \sum_{i=1}^{mk+2} w_{t_{j(k)}}^{(i)} \bar{H}_{(k)}^{(i)}(s), \tag{27}$$

$$\theta_{(k)} = \sum_{i=1}^{mk+2} w_{\theta_{(k)}}^{(i)} \bar{H}_{(k)}^{(i)}(s), \tag{28}$$

$$q_{(k)} = \sum_{i=1}^{mk+2} w_{q_{(k)}}^{(i)} \bar{H}_{(k)}^{(i)}(s), \tag{29}$$

where $s \in \Gamma_{(k)}$, mk is the number of training points on the segment k, $\{w_{u_{j(k)}}^{(i)}\}_{i=1}^{mk+2}$, $\{w_{t_{j(k)}}^{(i)}\}_{i=1}^{mk+2}$, $\{w_{\theta_{(k)}}^{(i)}\}_{i=1}^{mk+2}$ and $\{w_{q_{(k)}}^{(i)}\}_{i=1}^{mk+2}$ are the sets of weights of networks for the velocity $u_{j(k)}$, traction $t_{j(k)}$, temperature $\theta_{(k)}$ and normal flux $q_{(k)}$ respectively. Similarly, the geometry can be interpolated from the nodal values by using IRBFNs as

$$x_{1(k)} = \sum_{i=1}^{mk+2} w_{x_{1(k)}}^{(i)} \bar{H}_{(k)}^{(i)}(s), \tag{30}$$

$$x_{2(k)} = \sum_{i=1}^{mk+2} w_{x_{2(k)}}^{(i)} \bar{H}_{(k)}^{(i)}(s). \tag{31}$$

Substitutions of (26) and (27) into (24) and also (28) and (29) into (25) yield

$$\sum_{k=1}^{N_s} \int_{\Gamma_{(k)}} T_{ij}(\mathbf{y},\mathbf{x}) \left(\sum_{i=1}^{mk+2} w_{u_{j(k)}}^{(i)} \bar{H}_{(k)}^{(i)}(s) - \sum_{i=1}^{ml+2} w_{u_{j(l)}}^{(i)} \bar{H}_{(l)}^{(i)}(s_{\mathbf{y}}) \right) d\Gamma_{(k)}(s)$$
$$- \sum_{k=1}^{N_s} \int_{\Gamma_{(k)}} U_{ij}(\mathbf{y},\mathbf{x}) \left(\sum_{i=1}^{mk+2} w_{t_{j(k)}}^{(i)} \bar{H}_{(k)}^{(i)}(s) \right) d\Gamma_{(k)}(s) + VIm = 0, \tag{32}$$

$$\sum_{k=1}^{N_s} \int_{\Gamma_{(k)}} q^*(\mathbf{y},\mathbf{x}) \left(\sum_{i=1}^{mk+2} w_{\theta(k)}^{(i)} \bar{H}_{(k)}^{(i)}(s) - \sum_{i=1}^{ml+2} w_{\theta(l)}^{(i)} \bar{H}_{(l)}^{(i)}(s_{\mathbf{y}}) \right) d\Gamma_{(k)}(s)$$
$$- \sum_{k=1}^{N_s} \int_{\Gamma_{(k)}} u^*(\mathbf{y},\mathbf{x}) \left(\sum_{i=1}^{mk+2} w_{q(k)}^{(i)} \bar{H}_{(k)}^{(i)}(s) \right) d\Gamma_{(k)}(s) + VIe = 0, \tag{33}$$

or,

$$\sum_{k=1}^{N_s}\left\{\sum_{i=1}^{mk+2} w_{u_{j(k)}}^{(i)}\left(\int_{\Gamma_{(k)}} T_{ij}(\mathbf{y},\mathbf{x})\bar{H}_{(k)}^{(i)}(s)d\Gamma_{(k)}\right)-\sum_{i=1}^{ml+2} w_{u_{j(l)}}^{(i)}\left(\int_{\Gamma_{(k)}} T_{ij}(\mathbf{y},\mathbf{x})\bar{H}_{(l)}^{(i)}(s_{\mathbf{y}})d\Gamma_{(k)}\right)\right\}$$
$$-\sum_{k=1}^{N_s}\sum_{i=1}^{mk+2} w_{t_{j(k)}}^{(i)}\left(\int_{\Gamma_{(k)}} U_{ij}(\mathbf{y},\mathbf{x})\bar{H}_{(k)}^{(i)}(s)d\Gamma_{(k)}\right)+VIm=0, \tag{34}$$

$$\sum_{k=1}^{N_s}\left\{\sum_{i=1}^{mk+2} w_{\theta(k)}^{(i)}\left(\int_{\Gamma_{(k)}} q^{*}(\mathbf{y},\mathbf{x})\bar{H}_{(k)}^{(i)}(s)d\Gamma_{(k)}\right)-\sum_{i=1}^{ml+2} w_{\theta(l)}^{(i)}\left(\int_{\Gamma_{(k)}} q^{*}(\mathbf{y},\mathbf{x})\bar{H}_{(l)}^{(i)}(s_{\mathbf{y}})d\Gamma_{(k)}\right)\right\}$$
$$-\sum_{k=1}^{N_s}\sum_{i=1}^{mk+2} w_{q(k)}^{(i)}\left(\int_{\Gamma_{(k)}} u^{*}(\mathbf{y},\mathbf{x})\bar{H}_{(k)}^{(i)}(s)d\Gamma_{(k)}\right)+VIe=0, \tag{35}$$

where mk can vary from segment to segment. Equations (34) and (35) are formulated in terms of the IRBFN weights of networks for the functions rather than the nodal values of the functions as in the case of standard BEM. Clearly, the weakly singular integrals in (34) and (35) can be treated as in the case of standard BEM.

4.2 Decoupled approach

The process of locating the source point $\mathbf{y}$ at all boundary training points results in a system of nonlinear equations with the unknowns being the IRBFN weights. The decoupled approach is adopted here to handle this nonlinearity. At each iteration in this approach, the momentum and the energy equations are solved in two sequential steps, where BEM procedures for the viscous flow problem and the potential problem can be directly applied without any modification. For a given kinematics, the buoyant force is obtained by solving integral equations (35) (the energy equation). The kinematics are then updated by solving integral equations (34) (the momentum equation), and the procedure is iterated until a stopping criterion is satisfied. Hence, an attractive feature of this technique is that the requirement of core memory is significantly less than in the case of

coupled approaches, where the discretised governing equations are solved simultaneously for the whole set of primary variables, usually by means of Newton's iterative scheme in which the unknowns also contain internal values. In solving integral equations (34) and (35), the Picard's iterative algorithm is employed to render nonlinear terms linear.

4.3 Flow chart

The procedural flow chart can be briefly summarised as follows

1. Divide the boundary into a relatively small number of segments over each of which the boundary is smooth and the prescribed boundary conditions are of the same type;

2. Apply the IRBFN method for the approximation of the prescribed physical boundary conditions in order to obtain IRBFN weights which are the boundary conditions in the weight space;

3. Guess the initial temperature and velocity fields (usually initialised to zero in the present work);

4. Compute the pseudo body force VIm, which contains the buoyant force and the convective term, using the updated temperature and velocity fields;

5. Solve integral equation (34) (the momentum equation) for the new velocity field;

6. Compute the pseudo source function VIe in the Poisson's equation using the new velocity field obtained from the previous step;

7. Solve integral equation (35) (the energy equation) for the new temperature field;

8. Check for convergence. Convergence Measure (CM) at the kth iteration is measured as the norm of the relative difference of the velocity and temperature fields between

two successive iterations kth and $(k-1)$th. The solution procedure is terminated when $CM < tol$, where tol is a set tolerance (in this work $tol = 5.e-3$);

9. If not yet converged, repeat from the step 4; or exit if it is deemed that the procedure will not converge;

10. If converged, output the results.

Note that system matrices obtained here depend only on the geometry of the problem and hence the computation of the two inverse matrices in steps 5 and 7 needs be done only once at the first iteration for all subsequent iterations and also for all values of the Rayleigh number, provided that the mesh data are fixed. However, RHS vectors containing volume integrals change and need to be updated during the iterative process.

5 Natural convection in a square cavity

Natural convection in an enclosed cavity provides a means to test and validate numerical methods. The problem, which is in itself of considerable practical interest, is schematically shown in Figure 1. The domain of interest is a square cavity of a unit size, containing a Boussinesq fluid of Prandtl number of 0.71. Non-slip boundary conditions ($u_1 = 0, u_2 = 0$) are applied along all the walls. The left and right vertical walls are kept at temperatures $\theta_h = 1$ and $\theta_c = 0$, while the horizontal walls are insulated.

A number of uniform meshes, namely 11×11 (i.e. 11×4 boundary points and 9×9 internal points), 21×21, 31×31, 41×41 and 51×51 with the detail given in Table 1 are employed to study this problem for a wide range of values of the Rayleigh number from $1.0e4$ to $1.0e7$. The sizes of system matrices obtained are much smaller than those associated with the FDM and FEM. For example, with a mesh of 51×51, the matrix sizes corresponding to the energy and momentum equations are 204×212 and 408×424

respectively, while they are about 2601×2601 and 5202×5202 in the case of FEM (without pressure). The ratio of the matrix sizes between two the numerical methods is about 156. The boundary of domain is divided into 4 segments corresponding to the four edges of the cavity and on each segment, the set of boundary points becomes the set of centres and also the set of collocation points of the network. In order to be able to present the correct description of multivalued traction at the corner, the extreme centres on each segment are shifted into the segment by a 1/4 of the distance between two adjacent centres (Figure 1). General results for this problem in the form of velocity vector and isotherm plots are displayed in Figures 2 and 3 respectively, where Rayleigh number values range from $1.0e4$ to $1.0e7$ and finer meshes are used for higher Ra values. It can be seen that there is a very close agreement with results available in the literature. The temperature and velocity vector fields are skew-symmetric with regard to the geometric centre of the cavity (centro-symmetric). Furthermore, temperature boundary layers at the vertical walls appear to be thinner and the isotherms are nearly horizontal in the core flow as the Rayleigh number increases. Thin boundary layers are also observed for the flow close to the walls.

5.1 Mesh convergence

The use of the last three finer meshes can achieve convergence up to a high Rayleigh number of $Ra = 1.0e7$, while coarser meshes of 21×21 and 11×11 can only yield convergence at lower values of the Rayleigh number of $1.0e6$ and $1.0e5$, respectively. An important measure associated with this type of flow is the Nusselt number defined by

$$Nu(x_1) = \int_0^1 (u_1\theta - \theta_{,1})dx_2,$$

which is used here to study mesh convergence. Integrals here are computed using Simpson rule. Results obtained for the first three Rayleigh numbers and various mesh densities are displayed in Table 2, where the values of Nusselt numbers on the hot wall ($Nu_0 =$

$Nu(x_1 = 0)$) and throughout the cavity ($\bar{Nu} = \int_0^1 Nu(x_1)dx_1$) approach the benchmark solution of de Vahl Davis [6] as the mesh density increases. Unfortunately, the benchmark solution at a high Rayleigh number of $1.0e7$ was not available, and the present results are qualitatively compared with those obtained by FVM (Kaminski and Prakash [10]) and BDIE (Hribersek and Skerget [12]) as shown in Table 3, which is reasonable. To observe the behaviour of mesh convergence, the plot of the convergence rate is given in Figure 4. By regarding the solution on the finest mesh as "the exact one", errors in the Nusselt number on coarser meshes relative to the "exact solution" are computed and then shown in semi-logarithmic scale coordinate axes. For each Rayleigh number, the error obtained is consistently smaller as the mesh spacing decreases, which indicates the achievement of mesh convergence. With the same mesh size employed, the result at a lower Rayleigh number has a smaller error as expected. In the case of $Ra = 1.e4$, all errors obtained are less than 1% which means coarse meshes used here are adequate and able to capture the solution very well.

Another result to examine is the bulk continuity of the flow which is important for an overall quantitative sense of the solution accuracy (Aydin and Fenner [35]). For the cavity flow this is commonly achieved by computing the flow rate across the vertical plane passing through the geometric centre of the cavity as follows

$$Q = \frac{1}{Q_0} \left| \int_0^1 u_1(x_1 = 0.5, x_2) dx_2 \right|,$$

where Q_0 is the characteristic flow rate and chosen to be $Q_0 = \frac{1}{2}|(u_1)_{max}|1$ as in the case of the Couette flow. A more accurate solution would necessarily yield the flow rate closer to the exact value of zero. The flow rates for all Rayleigh numbers and various mesh sizes are shown in Table 4. The results show that the flow rates consistently tend to zero as the mesh density increases for all studied cases.

5.2 Solution accuracy

The present results are in good agreement with the benchmark solution, for example, errors in the Nusselt number throughout the cavity for the first three Rayleigh numbers (Table 2) are within 0.5 %. For a better view of the solution, variations of some important quantities for this type of flow are plotted. Firstly, the distribution of Nusselt numbers along the hot wall (Nu_0) and the vertical centreline ($Nu_{1/2}$) are presented in Figure 5 with the errors of the maximum value of Nu_0 being within 1.19% compared to the benchmark solution. Furthermore, the horizontal velocity profiles along the vertical centre line of the cavity and the vertical velocity profiles along the horizontal centreline are displayed in Figure 6, where errors of the maximum horizontal velocity are within 0.63% of the benchmark solution.

6 Natural convection in a horizontal concentric annulus

Natural convection in a horizontal concentric annulus, which is important in many engineering applications, is studied and reported in this section. The problem's geometry involves curved boundaries and therefore provides a means to validate further the present method. A comprehensive review of the investigations of this problem has been made by Kuehn and Goldstein [4]. Many solutions were obtained with $Pr = 0.7$ and $L/D_i = 0.8$, in which L is the gap width between the cylinders and D_i is the diameter of the inner cylinder. These conditions are also employed in the present work. Kuehn and Goldstein [4] reported the results at $Ra = 1.0e3$, $1.0e4$ and $5.0e4$ using FDM. Recently, Shu [2] provided the benchmark solution for Rayleigh numbers ranging from $1.0e2$ to $5.0e4$ using the differential quadrature method.

Since the flow is symmetric with respect to the vertical centreline, only half of the domain needs be taken as the computational domain. Figure 7 shows a schematic of domain together with volume discretisation and boundary conditions. The boundary is divided into 4 segments (two straight lines and two curves) with boundary conditions being

$$u_1 = 0, \quad t_2 = 0 \quad \text{and} \quad \theta_{,1} = 0$$

on the symmetry lines,

$$u_1 = 0, \quad u_2 = 0 \quad \text{and} \quad \theta = 0$$

on the outer cylinder and

$$u_1 = 0, \quad u_2 = 0 \quad \text{and} \quad \theta = 1$$

on the inner cylinder. Four uniformly distributed meshes, namely 11×21 (11 in the radial direction and 21 in the angular direction), 16×31, 21×41 and 31×61 for Rayleigh numbers $Ra = 1.0e3,\ 6.0e3,\ 1.0e4,\ 5.0e4$ are employed to study mesh convergence (Table 5). All meshes here are able to produce convergence at the highest Rayleigh number. Particularly, for a high $Ra = 5.0e4$, the use of only a coarse mesh of 11×21 seems to indicate that the IRBFN interpolation yields superior accuracy in solving PDEs. Results for this problem in the form of velocity vector and isotherm plots are shown in Figure 8 for various Rayleigh numbers and different meshes, which agree well with those of Kuehn and Goldstein [4]. As the Rayleigh number increases, the centre of rotation of the flow shifts upwards, while the temperature distribution resembles eccentric circles at the $Ra = 1.0e3$ and then becomes distorted with the appearance of thermal boundary layers near the lower portion of the inner cylinder and the top of the outer cylinder. Another important result is the average equivalent conductivity denoted by $\bar{k}_{eq}$. This quantity is defined as the actual heat flux divided by the heat flux that would occur by pure conduction in the

absence of fluid motion (Kuehn and Goldstein [4]) as follows

$$\bar{k}_{eq_i} = \frac{-\ln(R_o/R_i)}{\pi(R_o/R_i - 1)} \int_0^{\pi} \theta_{,r} d\phi$$

for the inner cylinder, and

$$\bar{k}_{eq_o} = \frac{-(R_o/R_i)\ln(R_o/R_i)}{\pi(R_o/R_i - 1)} \int_0^{\pi} \theta_{,r} d\phi$$

for the outer cylinder in which R_i and R_o are the radii of inner and outer cylinders respectively. Table 6 summarises the present results for various Rayleigh numbers using different meshes and those of Kuehn and Goldstein [4] obtained from the second order finite difference scheme and of Shu [2] obtained from the differential quadrature (DQ) method. The good agreement for both outer and inner cylinders can be seen between numerical methods. For each Rayleigh number, the mesh convergence of the average equivalent conductivity is very consistent and in addition the convergence rate is displayed in semi-logarithmic scale coordinate system in Figure 9. Variations of the local equivalent conductivity on cylinder surfaces in comparison with numerical results of Kuehn and Goldstein [4] are given in Figure 10, showing a close agreement.

7 Concluding remarks

This paper reports an effective BEM, through the introduction of 'universal approximator' neural networks into the standard BEM scheme to represent all boundary values including geometries, for the analysis of natural convection flow. A decoupled technique is adopted, where the momentum and energy equations are solved sequentially. The nonlinear terms are treated using Picard iteration with linear triangular cell approximation. The use of the decoupled approach and also the integral representation results in very small systems of equations in comparison with the FEM and FDM. High Rayleigh number solutions are

achieved with the use of relatively coarse and uniform mesh. Numerical results show the achievement of high convergence rate and a close agreement with previously published numerical solutions. The present IRBFN-BEM method is general and can be extended to solve other problems such as non-Newtonian fluid flow problems.

Acknowledgements

References

1. Mai-Duy N, Tran-Cong T. Numerical solution of Navier-Stokes equations using multiquadric radial basis function networks. *International Journal for Numerical Methods in Fluids* 2001; **37**:65-86.

2. Shu C. Application of differential quadrature method to simulate natural convection in a concentric annulus. *International Journal for Numerical Methods in Fluids* 1999; **30**:977-993.

3. Shu C, Zhu YD. Efficient computation of natural convection in a concentric annulus between an outer square cylinder and an inner circular cylinder. *International Journal for Numerical Methods in Fluids* 2002; **38**:429-445.

4. Kuehn TH, Goldstein RJ. An experimental and theoretical study of natural convection in the annulus between horizontal concentric cylinders. *Journal of Fluid Mechanics* 1976; **74**(4):695-719.

5. Projahn U, Rieger H, Beer H. Numerical analysis of laminar natural convection between concentric and eccentric cylinders. *Numerical Heat Transfer* 1981; **4**:131-146.

6. de Vahl Davis G. Natural convection of air in a square cavity: a bench mark numerical solution. *International Journal for Numerical Methods in Fluids* 1983; **3**:249-264.

7. Sammouda H, Belghith A, Surry C. Finite element simulation of transient natural convection of low-Prandtl-number fluids in heated cavity. *International Journal of Numerical Methods for Heat & Fluid Flow* 1999; **9**(5):612-624.

8. Manzari MT. An explicit finite element algorithm for convection heat transfer problems. *International Journal of Numerical Methods for Heat & Fluid Flow* 1999; **9**(8):860-877.

9. Glakpe EK, Watkins CB, Cannon JN. Constant heat flux solutions for natural convection between concentric and eccentric horizontal cylinders. *Numerical Heat Transfer* 1986; **10**:279-295.

10. Kaminski DA, Prakash C. Conjugate natural convection in a square enclosure: effect of conduction in one of the vertical walls. *International Journal for Heat and Mass Transfer* 1986; **29**(12):1979-1988.

11. Kitagawa K, Wrobel LC, Brebbia CA, Tanaka M. A boundary element formulation for natural convection problems. *International Journal for Numerical Methods in Fluids* 1988; **8**:139-149.

12. Hribersek M, Skerget L. Fast boundary-domain integral algorithm for the computation of incompressible fluid flow problems. *International Journal for Numerical Methods in Fluids* 1999; **31**:891-907.

13. Power H, Mingo R. The DRM sub-domain decomposition approach for two-dimensional thermal convection flow problems. *Engineering Analysis with Boundary Elements* 2000; **24**:121-127.

14. Banerjee PK, Butterfield R. *Boundary Element Methods in Engineering Science*. McGraw-Hill: London, 1981.

15. Brebbia CA, Telles JCF, Wrobel LC. *Boundary Element Techniques: Theory and Applications in Engineering*. Springer-Verlag: Berlin, 1984.

16. Pozrikidis C. *A Practical Guide to Boundary Element Methods with the Software Library BEMLIB*. Boca Raton: CRC Press, 2002.

17. Bush MB, Tanner RI. Numerical solution of viscous flows using Integral Equation Methods. *International Journal for Numerical Methods in Fluids* 1983; **3**:71-92.

18. Dargush GF, Banerjee PK. A boundary element method for steady incompressible thermoviscous flow. *International Journal for Numerical Methods in Engineering* 1991; **31**:1605-1626.

19. Partridge PW, Brebbia CA, Wrobel LC. *The Dual Reciprocity Boundary Element Method*. Southampton: Computational Mechanics Publications, 1992.

20. Zheng R, Coleman CJ, Phan-Thien N. A boundary element approach for non-homogeneous potential problems. *Computational Mechanics* 1991; **7**:279-288.

21. Onishi K, Kuroki T, Tanaka M. Boundary element method for laminar viscous flow and convective diffusion problems. In *Topics in Boundary Element Research, Vol. 2.*, Brebbia CA (ed); Springer-Verlag: Berlin, 1985; pp. 209-229.

22. Skerget P, Alujevic A, Kuhn G, Brebbia CA. Natural convection flow problems by BEM. In *Boundary Element IX*, Brebbia CA (ed); Computational Mechanics Publications: Southampton, 1987; pp. 401-417.

23. Kitagawa K. *Lecture Notes in Engineering. Vol. 55: Boundary Element Analysis of Viscous Flow*. Springer-Verlag: Berlin, 1990.

24. Mai-Duy N, Tran-Cong T. Mesh-free radial basis function network methods with domain decomposition for approximation of functions and numerical solution of Poisson's equations. *Engineering Analysis with Boundary Elements* 2002; **26**:133-156.

25. Mai-Duy N, Tran-Cong T. Approximation of function and its derivatives using radial basis function network methods. *Applied Mathematical Modelling* 2003; **27**:197-220.

26. Mai-Duy N, Tran-Cong T. Neural networks for BEM analysis of steady viscous flows. *International Journal for Numerical Methods in Fluids* 2003; **41**:743-763.

27. Haykin S. *Neural Networks: A Comprehensive Foundation.* Prentice-Hall: New Jersey, 1999.

28. Girosi F, Poggio T. Networks and the best approximation property. *Biological Cybernetics* 1990; **63**:169-176.

29. Park J, Sandberg IW. Universal approximation using radial basis function networks. *Neural Computation* 1991; **3**:246-257.

30. Power H, Partridge PW. The use of Stokes's fundamental solution for the boundary only formulation of the three-dimensional Navier-Stokes equations for moderate Reynolds numbers. *International Journal for Numerical Methods in Engineering* 1994; **37**:1825-1840.

31. Kansa EJ. Multiquadrics- A scattered data approximation scheme with applications to computational fluid-dynamics-II. Solutions to parabolic, hyperbolic and elliptic partial differential equations. *Computers and Mathematics with Applications* 1990; **19**(8/9):147-161.

32. Zerroukat M, Power H, Chen CS. A numerical method for heat transfer problems using collocation and radial basis functions. *International Journal for Numerical Methods in Engineering* 1998; **42**:1263-1278.

33. Mai-Duy N, Tran-Cong T. Numerical solution of differential equations using multiquadric radial basis function networks. *Neural Networks* 2001; **14**(2):185-199.

34. Telles JCF. A self-adaptive co-ordinate transformation for efficient numerical evaluation of general boundary element integrals. *International Journal for Numerical Methods in Engineering* 1987; **24**:959-973.

35. Aydin M, Fenner RT. Boundary element analysis of driven cavity flow for low and moderate Reynolds numbers. *International Journal for Numerical Methods in Fluids* 2001; **37**:45-64.

Table 1: Natural convection flow in a square cavity: a number of meshes are used for the study of convergence. Boundary points (B. points), internal points (I. points) and triangular elements (T. elements) together with matrix sizes are displayed. The matrix sizes obtained here are much smaller than those associated with FEM and FDM. For example, with a mesh of 51×51, the matrix sizes corresponding to the energy and momentum equations are 204×212 and 408×424 respectively, while they are about 2601×2601 and 5202×5202 in the case of FEM without pressure. The ratio of the matrix sizes between the two numerical methods is about 156.

Mesh	B. points	I. points	Tri. elements	Matrix size of (34)	Matrix size of (35)
11×11	11×4	9×9	208	44×52	88×104
21×21	21×4	19×19	808	84×92	168×184
31×31	31×4	29×29	1808	124×132	248×264
41×41	41×4	39×39	3208	164×172	328×344
51×51	51×4	49×49	5008	204×212	408×424

Table 2: Natural convection flow in a square cavity: comparison of Nusselt numbers a) on the hot wall (Nu_0) and b) throughout the cavity ($\bar{Nu}$) obtained by the present IRBFN-BEM for a range of $Ra = 1.e4 - 1.e6$ and the benchmark solution of de Vahl Davis [6] which shows a very close agreement.

IRBFN-BEM						Benchmark solution
Mesh	11×11	21×21	31×31	41×41	51×51	
$Ra = 1e+4$						
Nu_0	2.26	2.25	2.25	2.25	2.25	2.24
$\bar{Nu}$	2.26	2.25	2.25	2.25	2.25	2.24
$Ra = 1e+5$						
Nu_0	4.83	4.63	4.60	4.56	4.55	4.51
$\bar{Nu}$	4.47	4.53	4.53	4.53	4.53	4.52
$Ra = 1e+6$						
Nu_0	—	9.64	9.29	9.13	9.04	8.82
$\bar{Nu}$	—	8.45	8.68	8.75	8.79	8.80

Table 3: Natural convection flow in a square cavity: qualitative comparison of the Nusselt number throughout the cavity ($\bar{Nu}$) at $Ra = 1.0e7, Gr = 1.4e7$ obtained by the present IRBFN-BEM and those by BDIE (Hribersek and Skerget [12]) and FVM (Kaminski and Prakash [10]) at $Ra = 7.1e6, Gr = 1.0e7$.

	IRBFN-BEM ($Gr = 1.4e7$)			BDIE ($Gr = 1.0e7$)	FVM ($Gr = 1.0e7$)
Mesh	31×31	41×41	51×51	41×41	40×30
Nu	15.12	15.53	15.85	14.18	15.09

Table 4: Natural convection flow in a square cavity: the volumetric flow rate across the vertical mid-plane obtained by the present method. This quantity is defined by $Q = \frac{1}{Q_0}|\int_0^1 u_1(x_1 = 0.5, x_2)dx_2|$, where Q_0 is the characteristic flow rate and chosen to be $Q_0 = \frac{1}{2}|(u_1)_{max}|1$ as in the case of the Couette flow. For each Rayleigh number, the values tend to the exact value of zero as a mesh density increases which show that the characteristic of a mesh convergence is achieved. With the same mesh employed, it is expected that the error is smaller with reducing a Rayleigh number which are properly reflected through the decrement of the flow rate values here.

IRBFN-BEM						Exact solution
Mesh	11×11	21×21	31×31	41×41	51×51	
Q(Ra=1e+4)	$5.0e-3$	$2.8e-3$	$9.5e-4$	$4.5e-4$	$2.6e-4$	0
Q(Ra=1e+5)	$1.7e-2$	$1.0e-2$	$3.5e-3$	$1.7e-3$	$9.8e-4$	0
Q(Ra=1e+6)	—	$6.0e-2$	$2.1e-2$	$1.0e-2$	$6.0e-3$	0
Q(Ra=1e+7)	—	—	$9.5e-2$	$4.3e-2$	$2.5e-2$	0

Table 5: Natural convection flow in a horizontal concentric annulus: a number of meshes are used for the study of convergence. Boundary points (B. points), internal points (I. points) and triangular elements (T. elements) together with matrix sizes are displayed.

Mesh	B. points	I. points	Tri. elements	Matrix size of (34)	Matrix size of (35)
11×21	$(11+21) \times 2$	9×19	408	64×72	128×144
16×31	$(16+31) \times 2$	14×29	908	94×102	188×204
21×41	$(21+41) \times 2$	19×39	1608	124×132	248×264
31×61	$(31+61) \times 2$	29×59	3608	184×192	368×384

Table 6: Natural convection flow in a horizontal concentric annulus: comparison of the average equivalent conductivity obtained between the present IRBFN-BEM, the FDM (Kuehn and Glodstein [4]) and the DQ method (Shu [2]). The latter is regarded as the benchmark solution (Bench. sol.), which shows a very close agreement between the methods.

IRBFN-BEM					FDM	Bench. sol
Mesh	11×21	16×31	21×41	31×61		
$Ra = 1.0e+3$						
$\bar{k}_{eq_i}$	1.087	1.084	1.083	1.082	1.081	1.082
$\bar{k}_{eq_o}$	1.079	1.080	1.080	1.081	1.084	1.082
$Ra = 6.0e+3$						
$\bar{k}_{eq_i}$	1.790	1.747	1.732	1.722	1.736	1.715
$\bar{k}_{eq_o}$	1.785	1.735	1.721	1.715	1.735	1.715
$Ra = 1.0e+4$						
$\bar{k}_{eq_i}$	2.087	2.028	2.006	1.990	2.010	1.979
$\bar{k}_{eq_o}$	2.117	2.023	1.995	1.981	2.005	1.979
$Ra = 5.0e+4$						
$\bar{k}_{eq_i}$	3.224	3.095	3.043	2.9992	3.024	2.958
$\bar{k}_{eq_o}$	3.970	3.405	3.171	3.0210	2.975	2.958

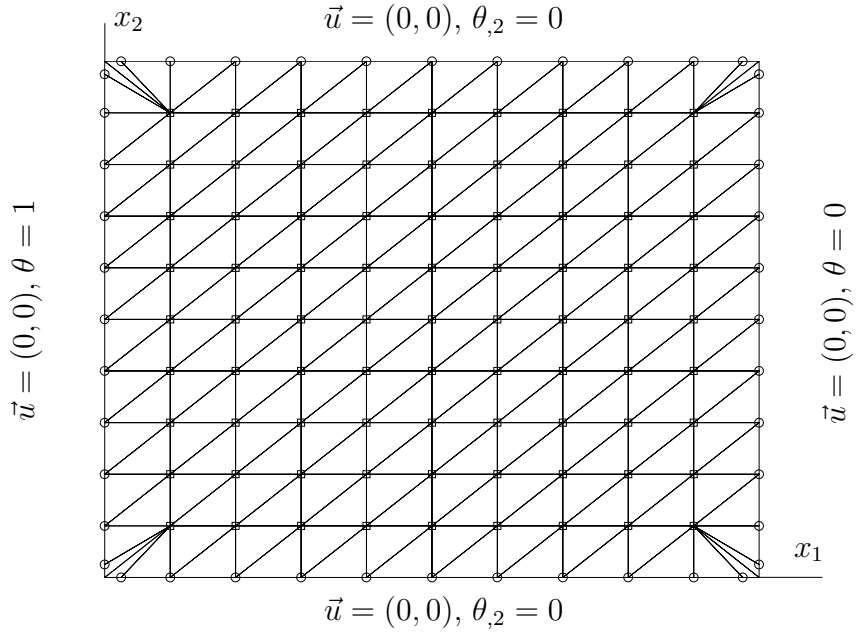

Figure 1: Natural convection flow in a square cavity: geometry definition, boundary condition and discretisation. Legends ∘: boundary point and □: internal point. The boundary is simply represented by the set of points (i.e. there are no boundary elements involved in variable interpolation). The volume cells are the same as in other comparative works cited in this paper.

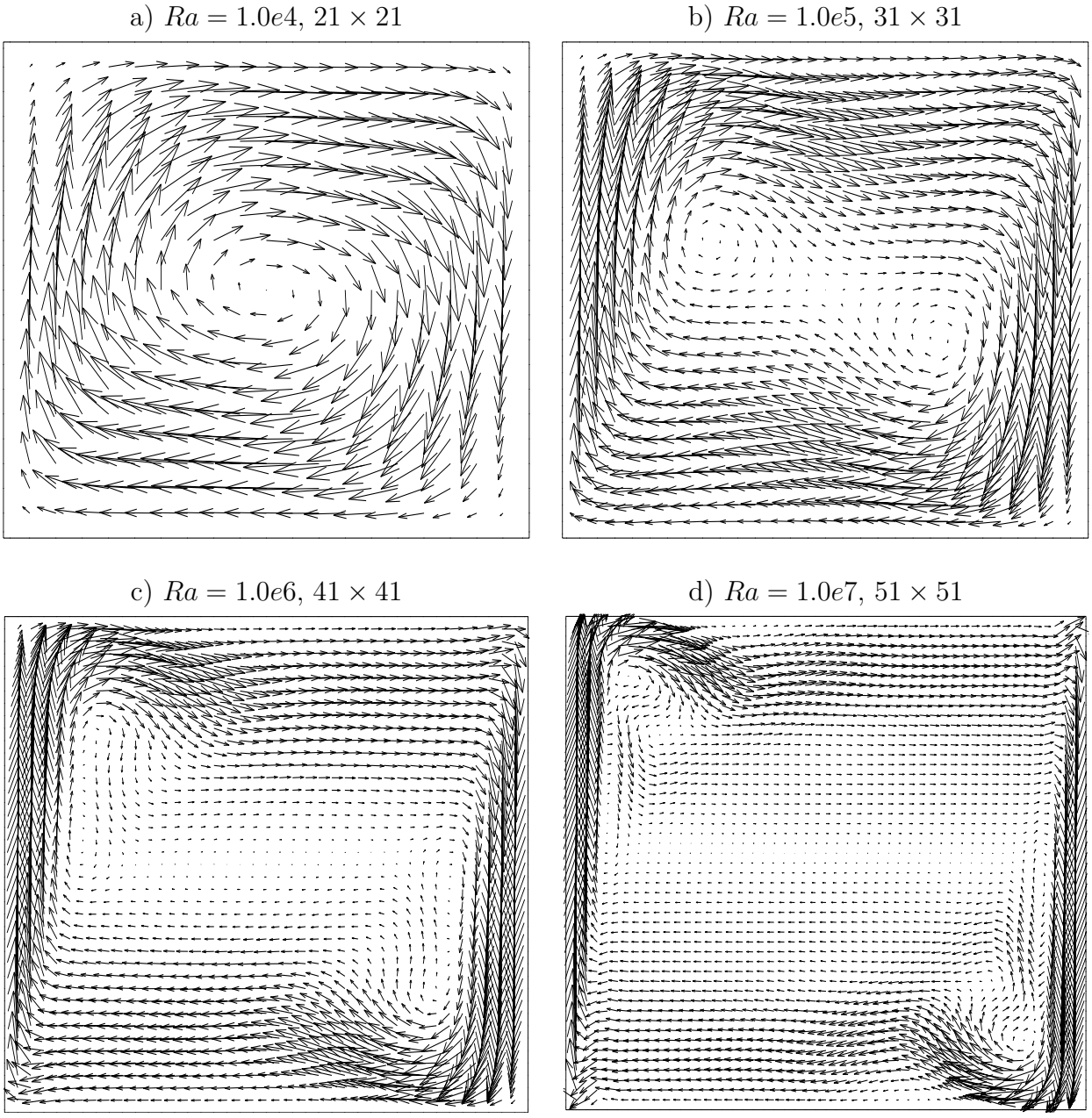

Figure 2: Natural convection flow in a square cavity: velocity fields. It can be seen that thin boundary layers appear for the flow close to the walls as the Rayleigh number increases. The mesh size is displayed for each Ra value.

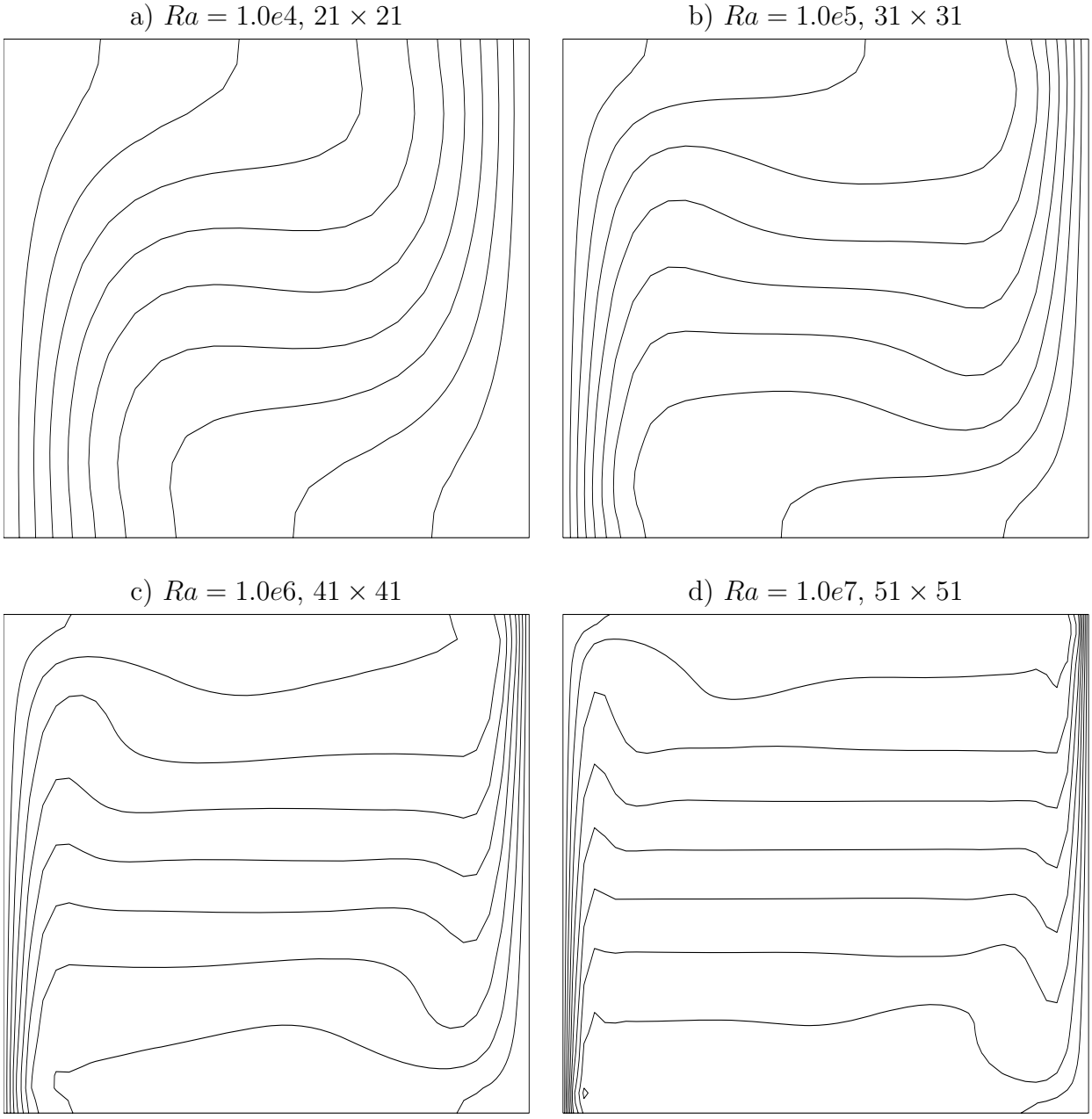

Figure 3: Natural convection flow in a square cavity: temperature fields. It can be seen that temperature boundary layers at the vertical walls appear to be thinner and the isotherms are nearly horizontal in the core flow as the Rayleigh number increases. The mesh size is displayed for each Ra value.

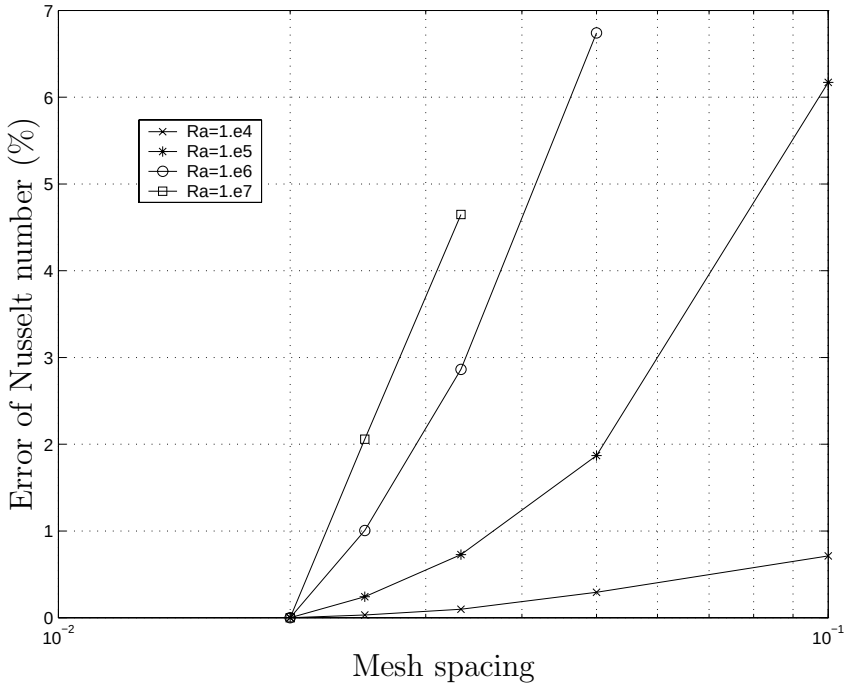

Figure 4: Natural convection flow in a square cavity: errors in the Nusselt number (%) computed on coarser meshes relative to the result on the finest mesh 51×51. For each Rayleigh number, the error here is consistently smaller as the mesh spacing decreases, which indicates the achievement of mesh convergence by the present method. With the same mesh density employed, the result at a lower Rayleigh number has a smaller error as expected. In the case of $Ra = 1.e4$, errors obtained are less than 1% which means coarse meshes used here are adequate and able to capture the solution very well.

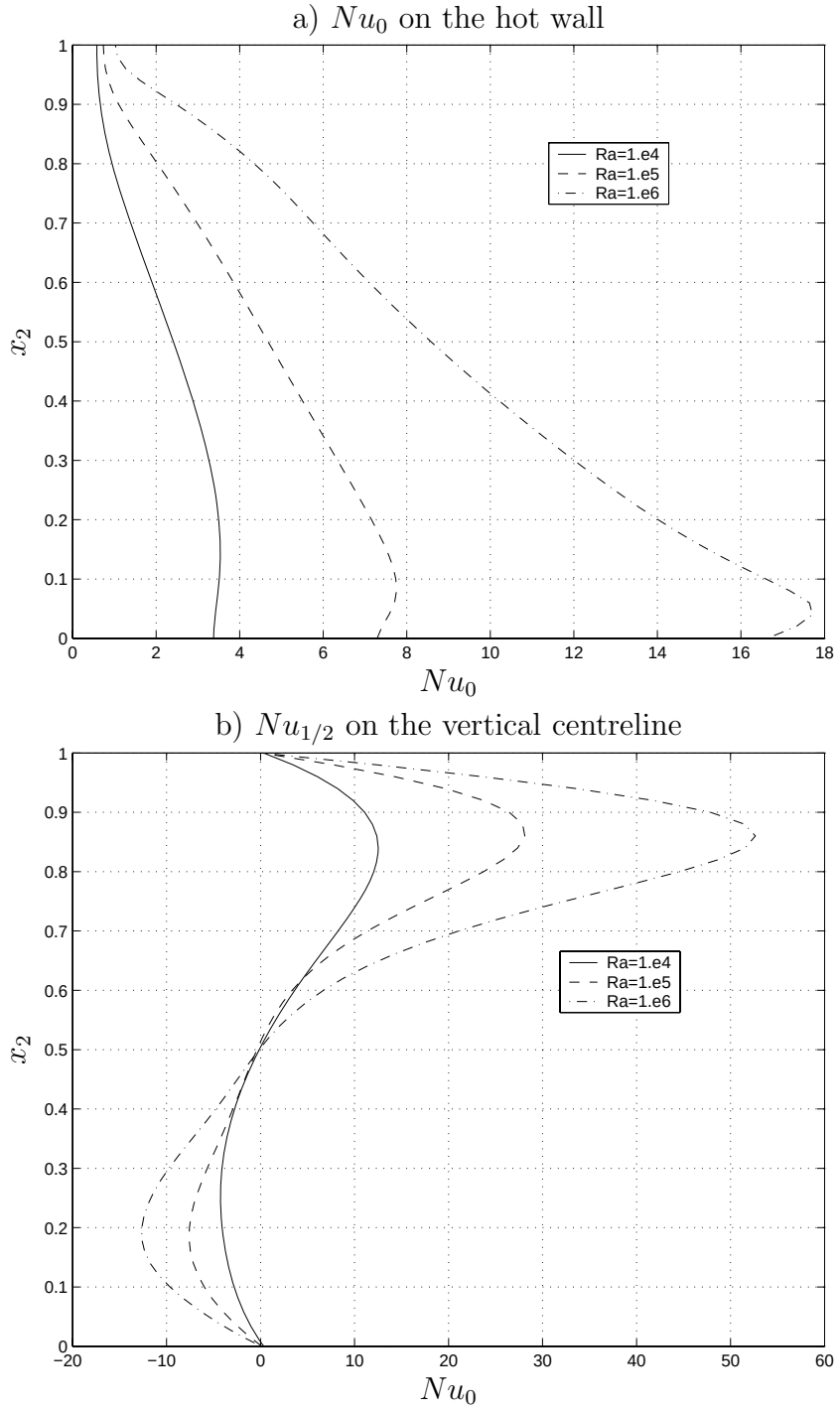

Figure 5: Natural convection flow in a square cavity: variations of Nusselt numbers along the hot wall and the vertical centreline for the fine mesh of 51×51. Errors of the maximum value of the Nusselt number on the hot wall for $Ra = 1.0e4$, $Ra = 1.0e5$ and $Ra = 1.0e6$ are, respectively, 0.21%, 0.50% and 1.19% compared to the benchmark solution.

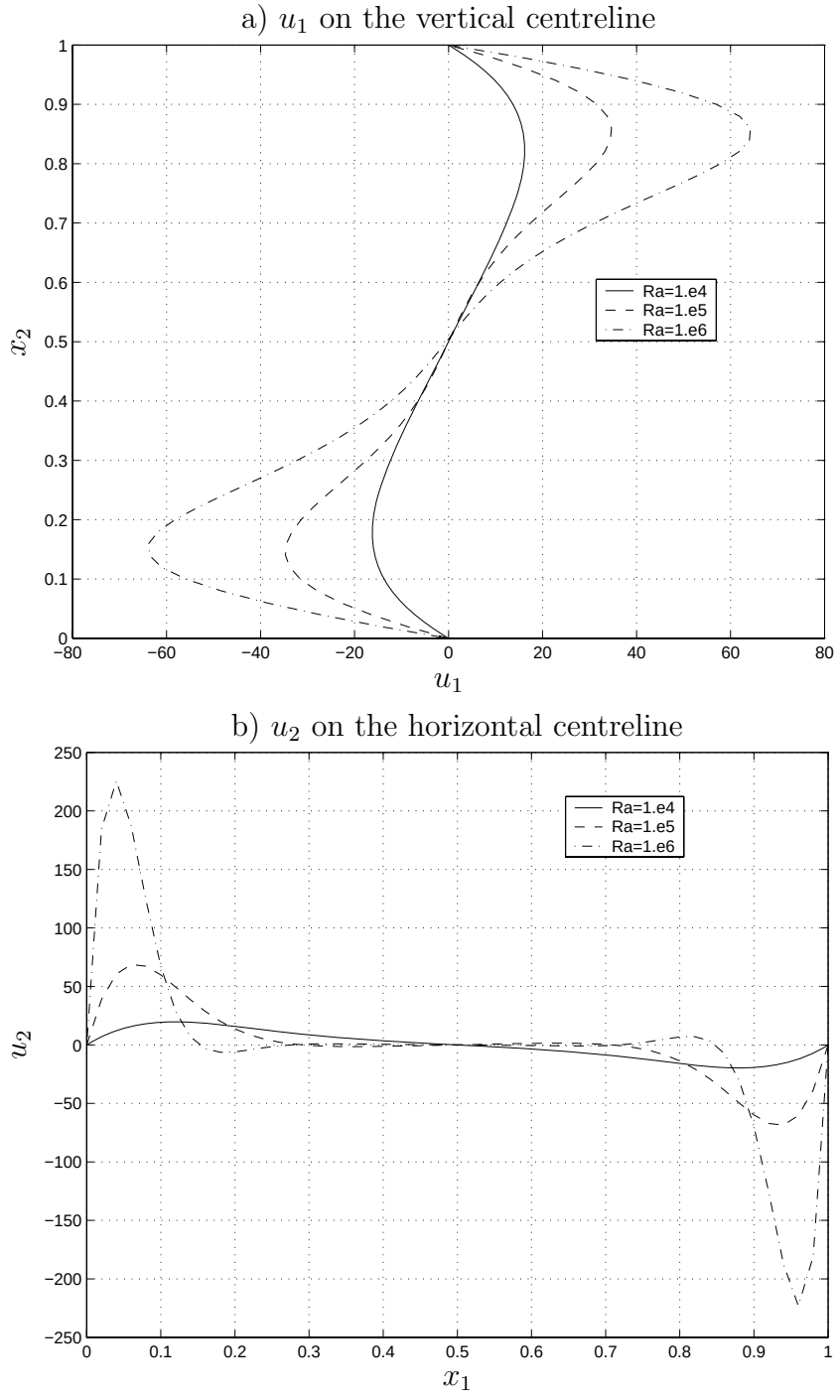

Figure 6: Natural convection flow in a square cavity: plots of velocity profiles along the vertical and horizontal centrelines for the fine mesh of 51×51. As the Rayleigh number is increased, boundary layers appear to be thinner.

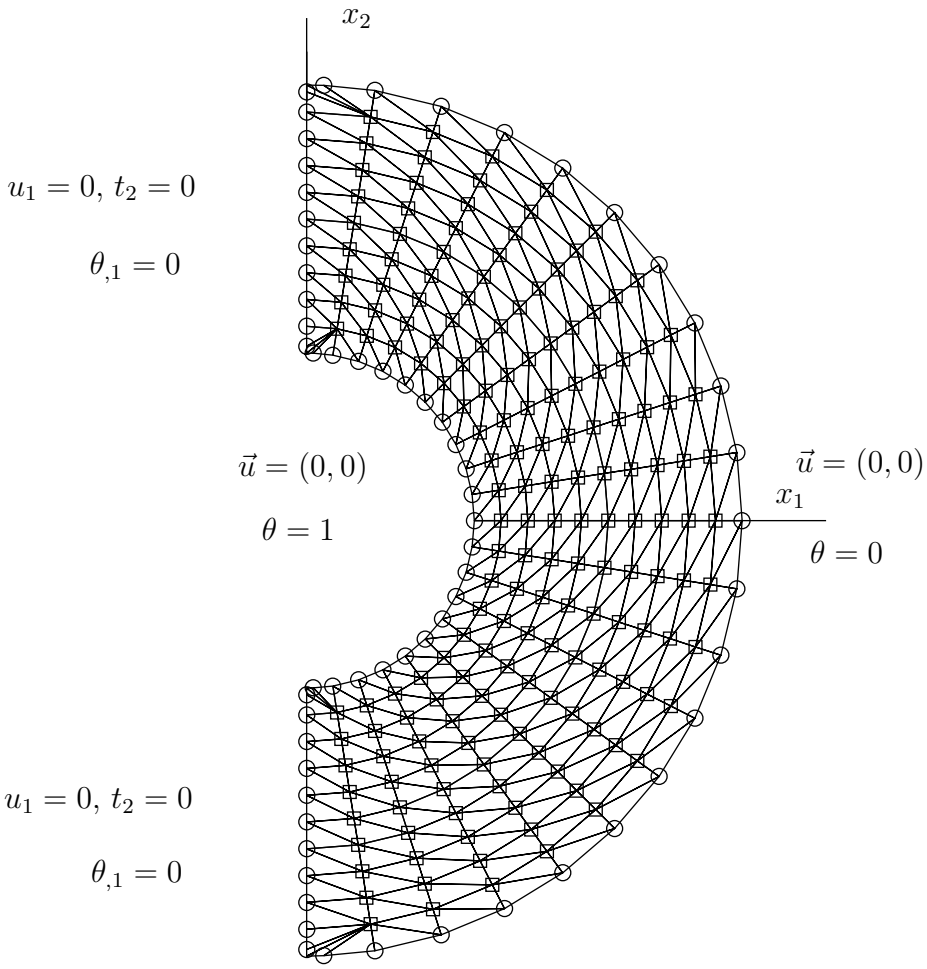

Figure 7: Natural convection flow in a horizontal concentric annulus: geometry definition, boundary condition and discretisation. Legends ∘: boundary point and □: internal point. The boundary is simply represented by the set of points (i.e. there are no boundary elements involved in variable interpolation). The volume cells are the same as in comparative works cited in this paper.

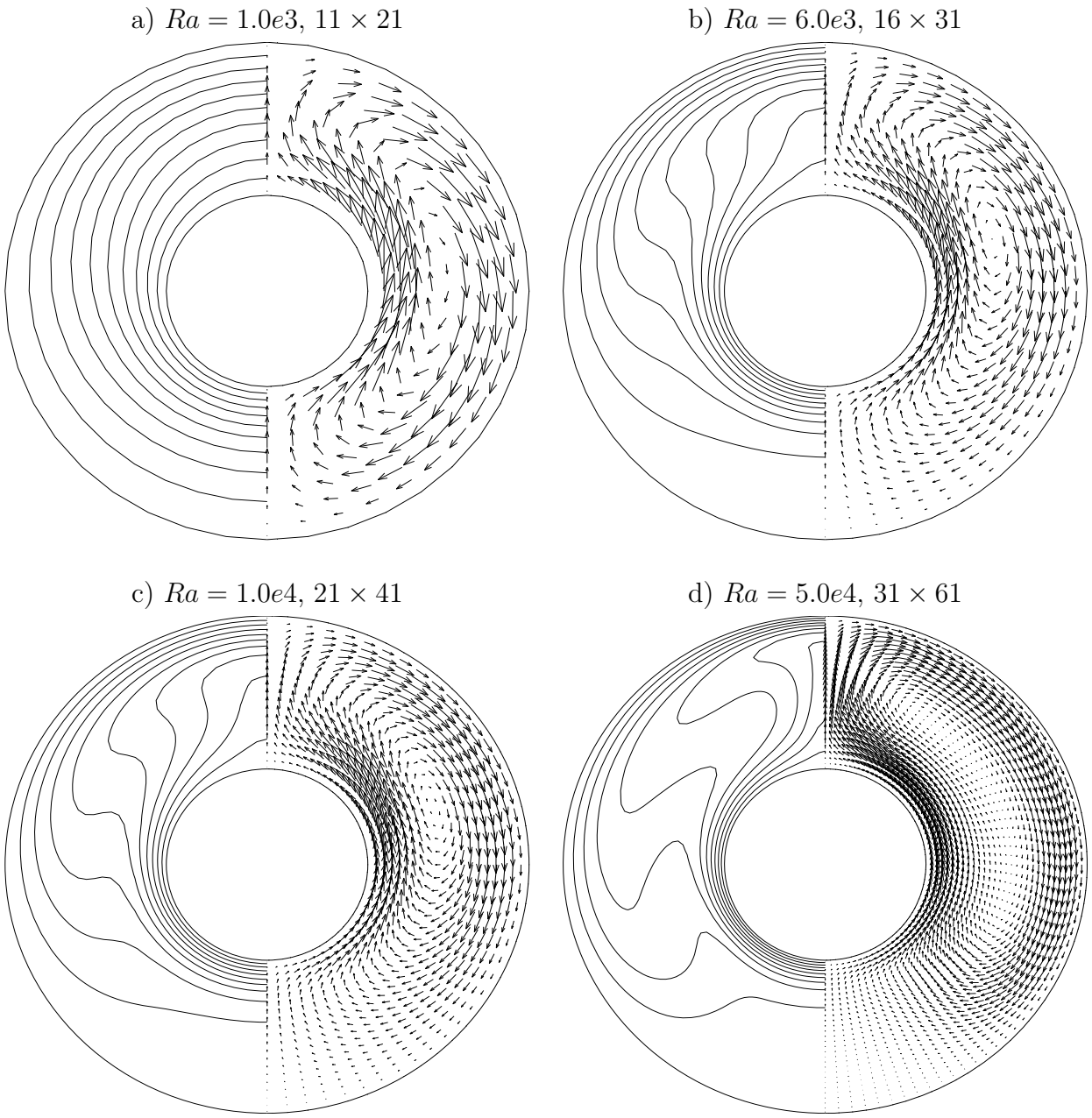

Figure 8: Natural convection flow in a horizontal concentric annulus: temperature and velocity vector fields. With an increase in the Rayleigh number, the centre of rotation of the flow shifts upwards, while the temperature distribution resembles eccentric circles at the $Ra = 1.0e3$ and then becomes distorted with the appearance of thermal boundary layers near the lower portion of the inner cylinder and the top of the outer cylinder.

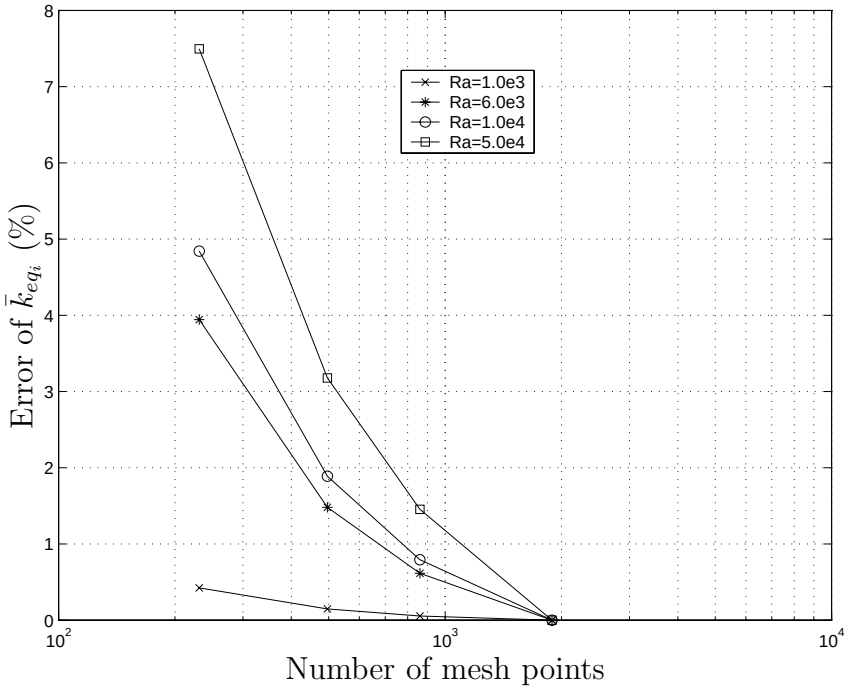

Figure 9: Natural convection flow in a horizontal concentric annulus: errors of the average equivalent conductivity (%) computed on coarser meshes relative to the result on the finest mesh 31×61. For each Rayleigh number, the error here is consistently smaller as the mesh density increases, which indicates the achievement of mesh convergence by the present method. With the same mesh density employed, a lower Rayleigh number has a smaller error as expected.

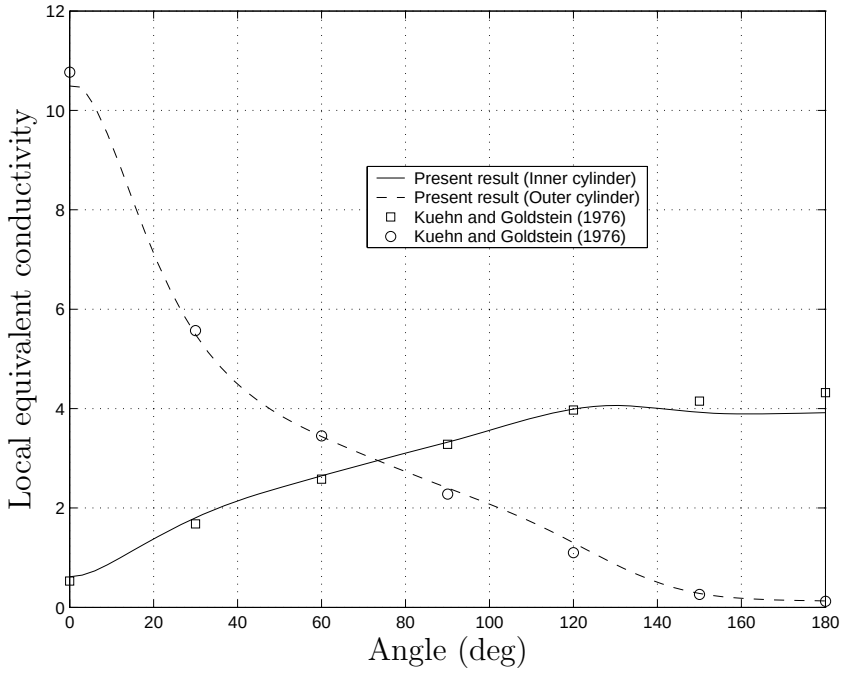

Figure 10: Natural convection flow in a horizontal concentric annulus ($Ra = 5.0e4$): Comparison of the local equivalent conductivity between the present method using a mesh of 31×61 and the FDM (Kuehn and Goldstein [4]) which shows a close agreement.